Available online at www.sciencedirect.com
SCIENCE DIRECT®
International Journal of Multiphase Flow 31 (2005) 223–237
International Journal of Multiphase Flow
www.elsevier.com/locate/ijmulflow

A computational study of the effect of initial bubble conditions on the motion of a gas bubble rising in viscous liquids

Mitsuhiro Ohta [a,*], Tatsuya Imura [a], Yutaka Yoshida [a], Mark Sussman [b]

[a] *Department of Applied Chemistry, Muroran Institute of Technology, 27-1 Mizumoto-cho, Muroran, Hokkaido 050-8585, Japan*
[b] *Department of Mathematics, Florida State University, Tallahassee, FL 32306, USA*

Received 6 February 2004; received in revised form 3 December 2004

Abstract

In order to examine the influence of initial bubble conditions on bubble rise motion, two-dimensional direct numerical simulations of the motion of a gas bubble rising in viscous liquids were carried out by a coupled level set/volume-of-fluid (CLSVOF) method. For dimensionless groups predicting a "spherical-cap bubble shape" (high Eötvös and low Morton numbers), we have found computationally that solutions depend on initial bubble conditions. Specifically, for spherical-cap bubble areas, we could obtain computational results of toroidal bubbles or spherical-cap bubbles depending on initial bubble conditions. On the other hand, we showed for low *Eo* and high *M* conditions that initial bubble conditions did not affect the final state of bubble rise motion.

Keywords: Numerical simulation; CLSVOF method; Bubble rising motion; Initial bubble condition

* Corresponding author.
E-mail address: mohta@mmm.muroran-it.ac.jp (M. Ohta).

0301-9322/$ - see front matter © 2004 Elsevier Ltd. All rights reserved.
doi:10.1016/j.ijmultiphaseflow.2004.12.001

1. Introduction

Gas–liquid two-phase flows in which gas bubbles are dispersed in viscous liquids are commonly encountered in various engineering processes (chemical reactors, nuclear power plants, bioreactors and combustion engines) as well as in nature. It is well identified that the dynamic behavior of gas bubbles in practical devices show very complicated motions. As is well known, Grace et al. (1976) and, in a more detailed study, Bhaga and Weber (1981) systematically arranged the motion of bubbles freely rising in viscous Newtonian liquids. They showed that the Reynolds (Re), Eötvös (Eo) and Morton (M) numbers were essential for describing a rising bubble (drop) or falling drop motion because shape and terminal velocity of a bubble or drop were determined by these three dimensionless numbers. At the same time, the fruits of their studies have provided important fundamental knowledge on the bubble rise motion. In the last decade, direct numerical simulation (DNS) has been recognized and used as an efficient technique for comprehending and revealing detailed flow structures and mechanisms for bubble motion in viscous liquids. As a consequence, many numerical studies of rising bubbles/drops have been presented (e.g., Tomiyama et al., 1994; Sussman and Smereka, 1997; Esmaeeli and Tryggvason, 1998, 1999; Himeno and Watanabe, 1999; Chen et al., 1999; Li et al., 2000; Son, 2001; Bunner and Tryggvason, 2002; Ohta et al., 2003, 2004). So far, most of the numerical simulations on bubble rise motion have been devoted to bubble rise dynamics with "intermediate" shape deformations and "intermediate" rise speeds. In other words, computations have not been sufficiently made for the rising bubble with large deformations, such as "skirted" and "spherical-cap" shapes and for the rising bubble with large Re.

Recently, as a very intriguing study, Wu and Gharib (2002) reported that small air bubbles of diameter range 1–2 mm rising in clean water have two steady shapes; a sphere and an ellipsoid. Along the same line, Tomiyama et al. (2002) showed experimentally that air bubbles rising through pure and contaminated water in a surface tension force dominant regime were largely influenced by an initial shape deformation. In terms of the Eo and M numbers, the conditions of their study correspond to low Eo and very low M regions. We remark that the numerical results of Yang et al. (2003) conflict with the experimental studies by Wu and Gharib (2002) and Tomiyama et al. (2002). Yang et al. (2003) report results using 2d-computations (a boundary fitted numerical method) which are initial-condition independent, whereas Wu and Gharib (2002) and Tomiyama et al. (2002) report results which are initial-condition dependent. We take the stance that 3d-computations are required for checking the initial shape dependence for such low Eo and very low M regions. With the studies of Wu and Gharib (2002), Tomiyama et al. (2002) and Yang et al. (2003) in mind, let us now reconsider the numerical results of bubble rising motion for high Eo and low M regions. The high Eo, low M region corresponds to the spherical-cap bubble area in the correlation diagram presented by Grace et al. (1976) and Bhaga and Weber (1981). Conversely, a toroidal shaped bubble, quite different from the spherical-cap bubble, has been numerically reproduced using parameters from the high Eo and low M region (e.g., Tomiyama et al., 1991; Sussman and Smereka, 1997; Chen et al., 1999). So, it would be incorrect to say that a toroidal bubble reproduced numerically is an improper result. We remark that toroidal air bubbles in water have been generated by Walters and Davidson (1963). Also, toroidal bubbles have been observed in the context of Dolphin play by Marten et al. (1996). One hypothesis for the cause of toroidal bubble formation versus cap bubble formation is due to the fact that at high

Eo number, an initial bubble whose shape is sufficiently different from a cap shape, will become unstable resulting in the break-up into a toroidal bubble (see Clift et al., 1978, pp. 339–342), regarding bubble instability). For the case of a bubble collapsing near a solid wall (Best, 1993), a toroidal bubble will form due to the lack of mobility of the portion of the bubble nearest the wall.

Based on previous literature, we shall focus on the effect of initial bubble conditions on the motion of a gas bubble rising in viscous liquids for high *Eo* and low *M* regions. We remark that Sussman and Smereka (1997), have shown a few results indicating initial condition dependence on the final shape, but their study was not in-depth. The objective of the present study is to computationally investigate how initial bubble conditions influence the final state of spherical-cap bubble rising motion. This present study was considered using 2d-axisymmetric computations based on a coupled level-set/volume-of-fluid (CLSVOF) method (Sussman and Puckett, 2000; Sussman, 2003).

2. Numerical analysis

2.1. The CLSVOF method

In this study, we use the CLSVOF method in order to represent and track the interface. The CLSVOF method is a robust numerical technique that combines some of the advantages of the volume-of-fluid (VOF) method (Hirt and Nichols, 1981; Puckett et al., 1997) with the level-set (LS) method (Sussman et al., 1994, 1998). In the VOF method, the volume-of-fluid function F is used to represent the interface. The values of F correspond to the volume fraction of liquid in a given computational cell. In other words, $F = 0$ when a computational cell contains only gas and $F = 1$ when a computational cell contains only liquid. If $0 < F < 1$, then a computational cell contains both gas and liquid phases. The VOF method has a great advantage that we can use accurate algorithms for advecting F so that mass is conserved while still maintaining a sharp representation of the interface. Meanwhile, the disadvantage of the VOF method is the fact that tangled and difficult reconstruction procedures are required for determining the slope of the piecewise linear VOF reconstructed interface. In the LS method, a smooth level-set (distance) function ϕ is used to track the interface. The interface is implicitly represented by the set of points in which $\phi = 0$. Liquid and gas regions are defined as $\phi > 0$ in the liquid and $\phi < 0$ in the gas, respectively. One of the advantages of the LS method is that we can track and present smoothly the interface. Also, the LS method allows for computations of two-phase flows with large density and/or viscosity ratios. However, the LS method has the disadvantage that mass is not explicitly conserved. As a result, we couple the LS function to the VOF function during the reinitialization process. The CLSVOF method is comprised of a best mix of the advantages of both the VOF and the LS methods. In the CLSVOF method, the coupling between the LS function and the VOF function occurs when computing the normal of the reconstructed interface in the VOF calculation process and also when assigning the LS function with the exact signed normal distance to the reconstructed interface in the LS calculation process. That is, the piecewise linear approximation (the volume-of-fluid reconstruction step) for the VOF method is determined using the unit normal vector $\boldsymbol{n}$ estimated from information of the LS function. In this process, the volume fractions are

truncated by use of the LS function, and spurious volumes are tactfully removed. Also, the reinitialized process (correction for losses and gains in mass) for the LS method is achieved through the use of the reconstructed interface of the VOF method at each new time step. At $t = 0$, F is initialized in each computational cell $\Omega_{i,j}(=(x,y)|x_i \leqslant x \leqslant x_{i+1}$ and $y_j \leqslant y \leqslant y_{j+1})$ to be

$$F_{i,j} = \frac{1}{\Delta x \Delta y} \int_{\Omega_{i,j}} H(\phi(x,y,0))\,\mathrm{d}x\,\mathrm{d}y. \tag{1}$$

Here, $H(\phi)$ is the Heaviside function,

$$H(\phi) = \begin{cases} 1 & \phi \geqslant 0, \\ 0 & \text{otherwise.} \end{cases} \tag{2}$$

2.2. Governing equations

In our study, the two-phase fluid flow is composed of air and a viscous Newtonian liquid. We assume that the flow in the air and liquid is incompressible. Also, we shall only consider axisymmetrical problems in 2d-cylindrical coordinates (r, z). Both incompressible fluids are governed by the continuity equation and momentum equations and the governing equations based on the CLSVOF method to be solved are as follows:

$$\nabla \cdot \boldsymbol{u} = 0 \tag{3}$$

$$\frac{\partial \boldsymbol{u}}{\partial t} + \nabla \cdot (\boldsymbol{u}\boldsymbol{u}) = -\frac{\nabla p}{\rho(\phi)} + \frac{1}{\rho(\phi)} \nabla \cdot \left[\mu\left(\nabla \boldsymbol{u} + \nabla \boldsymbol{u}^{\mathrm{T}}\right)\right] - \frac{\sigma\kappa(F)}{\rho(\phi)} \nabla H_\varepsilon(\phi) + \boldsymbol{g}, \tag{4}$$

where $\boldsymbol{u}$ expresses velocity of the fluid, t is the time, p is the pressure, μ is the viscosity, ρ is the density, σ is the surface tension coefficient and κ is the curvature of the interface. The curvature at $\phi = 0$ is computed to second-order accuracy using the VOF function (Sussman, 2003); the method is based on reconstructing the height function directly from the VOF function. $H_\varepsilon(\phi)$ is a smoothed Heaviside function which is introduced to avoid the sharp changes in pressure and diffusion term at the interface due to large density and/or viscosity ratios. The smoothed Heaviside function is defined as

$$H_\varepsilon(\phi) = \begin{cases} 1 & \phi > \varepsilon, \\ \frac{1}{2}[1 + \phi/\varepsilon + (1/\pi)\sin(\pi\phi/\varepsilon)] & |\phi| \leqslant \varepsilon, \\ 0 & \phi < -\varepsilon. \end{cases} \tag{5}$$

Here, ε is the interface numerical thickness which can be one of $1.0\,\Delta x$, $2.0\,\Delta x$ or $3.0\,\Delta x$. Note: Δx refers to the size of the finest mesh (see Section 3.2). We will describe the details of the interface numerical thickness in Chapter 4.

The term $\sigma\kappa(F)$ in the dynamic momentum equation (Eq. (4)) represents the surface tension-induced pressure jump.

Since the interface moves with the fluid particles, the evolution of F and ϕ are given as follows:

$$\frac{\partial F}{\partial t} + \nabla \cdot (\boldsymbol{u}F) = 0, \tag{6}$$

$$\frac{\partial \phi}{\partial t} + \nabla \cdot (\boldsymbol{u}\phi) = 0. \tag{7}$$

Since the density and viscosity are constant in each fluid, with a jump at the zero level of ϕ, they can be expressed as

$$\rho(\phi) = \rho_{\mathrm{G}}(1 - H_{\varepsilon}(\phi)) + \rho_{\mathrm{L}} H_{\varepsilon}(\phi) \tag{8}$$

and

$$\mu(\phi) = \mu_{\mathrm{G}}(1 - H_{\varepsilon}(\phi)) + \mu_{\mathrm{L}} H_{\varepsilon}(\phi), \tag{9}$$

where the subscripts G and L refer to the gas and liquid phases, respectively.

The governing equations are solved through a hydrodynamic scheme with second-order accuracy (Sussman and Puckett, 2000; Sussman, 2003). Note: the treatment of the interface numerical thickness and the interface pressure boundary condition are first order accurate because of the necessary smoothing of the Heaviside function. In our study, the spatial discretization uses second-order finite difference techniques. The discrete variables p, ϕ and F are located at the cell centers and the discrete variable $\boldsymbol{u}$ is located at face centers. We will briefly explain our numerical method below:

- Velocity and pressure fields are computed based on the variable density approximate projection method.
- The discretization of the advection term in Eq. (4) uses a second-order upwind predictor–corrector method based on the unsplit Godunov method.
- The time stepping procedure is based on the second-order Runge–Kutta method for the advection term and the second order Crank–Nicholson method for the viscous term.
- The interface curvature at $\phi = 0$ is estimated using the VOF function with second-order accuracy.
- The CLSVOF advection step is based on second-order operator split advection algorithms for both the LS and VOF functions (Eqs. (3) and (4)).

Finally, the solution was advanced through time in finite size steps which are limited in magnitude by various numerical stability considerations.

3. Computational system

3.1. Problem formulation

Computational targets in our study are shown in Fig. 1. Fig. 1 is a correlation map (Bhaga and Weber, 1981) relating terminal bubble shape to three dimensionless numbers: $Re(=\rho_{\mathrm{L}} D V/\mu_{\mathrm{L}}$, D: bubble diameter, V: bubble rise speed), $Eo(=\Delta\rho D^2 g/\sigma$, $\Delta\rho$: $\rho_{\mathrm{L}} - \rho_{\mathrm{G}})$ and $M(=\Delta\rho\mu_{\mathrm{L}}^4 g/\rho_{\mathrm{L}}^2\sigma^3)$. In Fig. 1, the black circles, squares and triangles are calculated points. The black squares show that the toroidal bubble could be numerically obtained when we started the computations from a spherical bubble. The black circles and triangles mean that we could obtain bubbles with an appropriate shape from the computations of a spherical bubble. For the triangle points, we

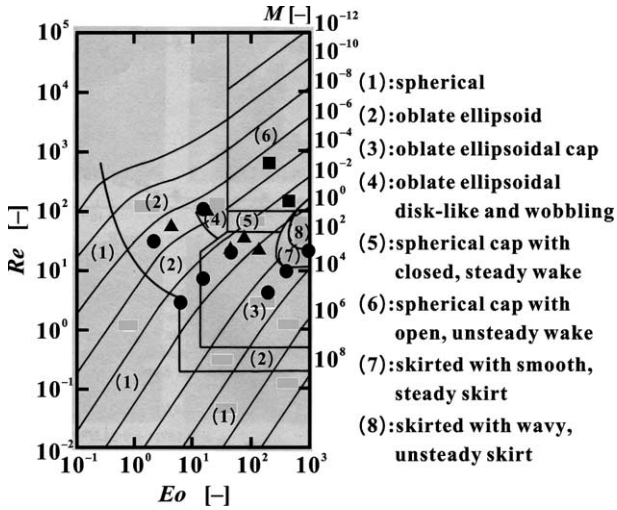

Fig. 1. The graphical correlation on bubble rise motion by Bhaga and Weber (1981).

compared our computations to previous experimental and numerical results. We will analyze all results in Chapter 4. In our study, physical properties of real gas–liquid systems were introduced in the computations. To be more precise, we used physical properties of silicone oil–air and mineral oil–air systems as two-phase fluids: silicone oil 10–air ($M = 9.9 \times 10^{-6}$), silicone oil 100–air ($M = 9.6 \times 10^{-2}$), silicone oil 1000–air ($M = 9.4 \times 10^{2}$) and mineral oil–air ($M = 6.5 \times 10^{-2}$) fluids. The silicone oil fluids are manufactured by Shin-Etsu Chemical Co., Ltd., and we have frequently used them in our experiments (e.g., Ohta et al., 2003). The mineral oil–air system was quoted from the study of Hnat and Buckmaster (1976). For such fluid systems, the density ratio between phases was on the order of about 800 and the viscosity ratio reached ~50,000. The computational domain for the 2d-axisymmetric computations is indicated schematically in Fig. 2. The computational domain has a r-directional dimensionless length L (=1.5) and a z-directional dimensionless height H (=4.5).

The chief purpose in this study is to examine the influence of initial bubble conditions on the final state of bubble rising motion. To achieve our goal, we shall consider bubble motions in which computations are either started from a spherical bubble or from deformed bubbles. In

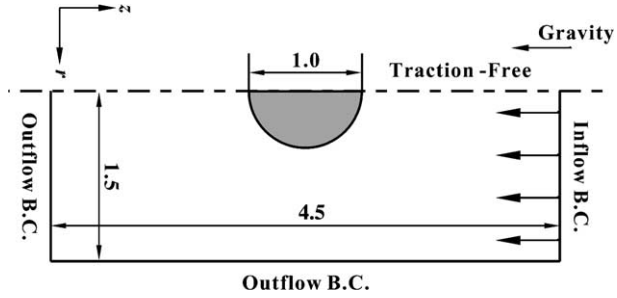

Fig. 2. Computational system.

beginning with a spherical bubble, as shown in Fig. 2, the spherical bubble was artificially imposed at the midpoint of the z-axis in the initial setting. Also, in order to establish a deformed initial bubble geometry, other than that of the spherical bubble, we started our computations using data from a previous computation of a deformed bubble. Details of these conditions will be illustrated in Chapter 4.

3.2. Numerical conditions

In the computations, conventional fixed grid algorithms require excessive computational resources (e.g., CPU speed and memory). We use adaptive mesh refinement (AMR) (Sussman et al., 1999) which allows us to save on computational resources by dynamically placing fine grids at the bubble interface. AMR enables us to increase the grid resolution at the regions near the interface. Fig. 3 shows a schematic diagram of the AMR system. The left side of Fig. 3 is an example of the grid structure in the AMR system. The right side of Fig. 3 is a computational example for a 2d-axisymmetric bubble using the AMR system. The mesh hierarchy is composed of different levels of refinement ranging from coarsest ($\ell = 0$, we label as "Level 0") to finest ($\ell = \ell_{\max}$). In Fig. 3, three levels (Level 0, Level 1 and Level 2) are indicated and the refinement ratio between the levels is two. Thus we have $\Delta x^{\ell+1} = 0.5\Delta x^{\ell}$. In order to validate our numerical scheme, we performed grid refinement studies for the bubbles with $Eo = 907$, $M = 9.4 \times 10^{2}$ ($D = 4.5 \times 10^{-2}$ m) and $Eo = 182$, $M = 9.9 \times 10^{-6}$ ($D = 2.0 \times 10^{-2}$ m). The reason for the choice of $Eo = 907$, $M = 9.4 \times 10^{2}$ ($D = 4.5 \times 10^{-2}$ m) is that it is the largest diameter in our study and the final shape of the bubble is considerably deformed (skirted bubble) based on Fig. 1. The reason why we selected $Eo = 182$, $M = 9.9 \times 10^{-6}$ ($D = 2.0 \times 10^{-2}$ m) is that this system has the largest Re value. Note that the results for $Eo = 182$, $M = 9.9 \times 10^{-6}$ ($D = 2.0 \times 10^{-2}$ m) were obtained in starting from a deformed initial bubble. As is shown in Fig. 4, the computed Re number depending on dimensionless time ($=tV/D$) is converged when going from a coarse grid computation (dimensionless mesh size, $\Delta x^{\ell_{\max}} = 1.17 \times 10^{-2}$) to a fine grid computation (dimensionless mesh size, $\Delta x^{\ell_{\max}} = 5.9 \times 10^{-3}$). As a result, we can conclude that our study performed using a dimensionless mesh size less than $\Delta x^{\ell_{\max}} = 1.17 \times 10^{-2}$ is a sufficiently sound system. We note that,

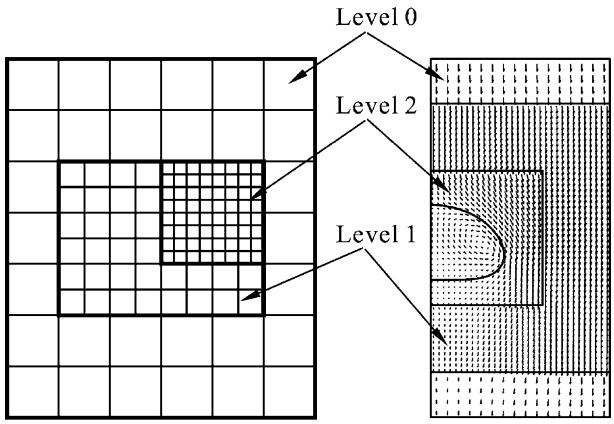

Fig. 3. Grid structure using the AMR system.

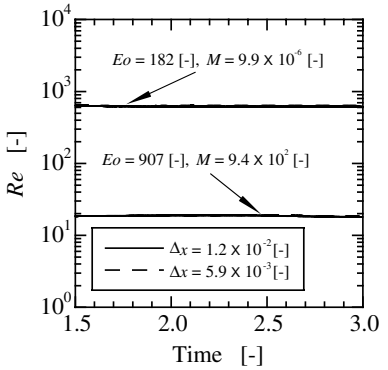

Fig. 4. The time evolution of Re depending on grid resolutions for the condition of $Eo = 182$, $M = 9.9 \times 10^{-6}$ and $Eo = 907$, $M = 9.4 \times 10^{2}$.

for a dimensionless mesh size of 1.17×10^{-2}, there are about 85 cells per bubble diameter. The physical boundary conditions for our bubble computations were as follows: inflow at the top wall, outflow boundaries at the bottom and right walls, and reflecting boundary condition at the axisymmetric center ($r = 0$).

4. Results and discussion

4.1. Validation against established numerical and experimental results

First, we validated our numerical method by comparing to previous numerical and experimental results. Fig. 5 shows comparison for five cases expressed by the triangles in Fig. 1: (a) the condition of $Re = 50$, $We\ (=\rho_L V^2 D/\sigma) = 4$ presented by Ryskin and Leal (1984); (b) the condition of $Re = 100$, $We = 10$ presented by Ryskin and Leal (1984); (c) the condition of $Eo = 116$, $M = 5.5$ presented by Bhaga and Weber (1981); (d) the condition of $Eo = 39$, $M = 6.5 \times 10^{-2}$ presented by

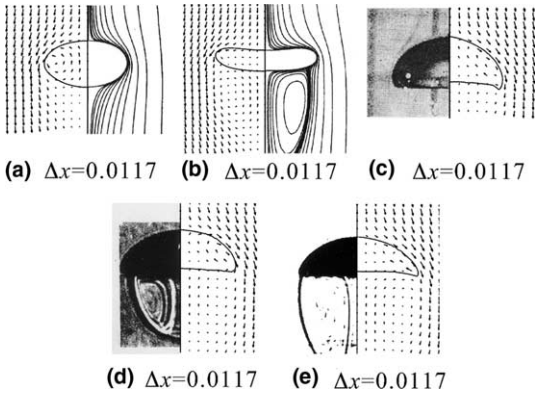

Fig. 5. Comparisons of our numerical results with numerical and experimental results in the prevailing literature.

Hnat and Buckmaster (1976); and (e) the condition of $Eo = 73$, $M = 6.5 \times 10^{-2}$ by Hnat and Buckmaster (1976). The left side is the computational result for cases (a) and (b), and the computational result is drawn at the right side for the other cases. All the numerical results shown in Fig. 5 were obtained using $\varepsilon = 1.0\Delta x$ and a spherical initial bubble. As is clear from Fig. 5, our numerical results of the bubble shape agree well with previous numerical and experimental results. In regard to *Re*, our computed *Re* values divided by *Re* values of the previous studies were 1.004 for case (a), 0.919 for case (b), 1.068 for case (c), 0.979 for case (d) and 0.970 for case (e). Thus, it can be confirmed that our computational method is in very good match with previous results (bubbles except for high *Eo* and low *M* areas).

4.2. Rising bubbles except for high Eo and low M areas

Fig. 6 presents a number of snapshots of bubble shapes except for high *Eo* and low *M* ("spherical-cap" bubble) regions after enough time has passed and the bubble shape has reached its terminal shape. All the results shown in Fig. 6 were obtained computationally using the initial condition of a spherical bubble shape. The numerical thickness conditions of $\varepsilon = 2.0\Delta x$ or $3.0\Delta x$ were used for these computations. One example is shown in Fig. 6 that lies in the high *Eo* and low *M* ($Eo = 182$ and $M = 9.9 \times 10^{-6}$) region. In the case of $Eo = 182$ and

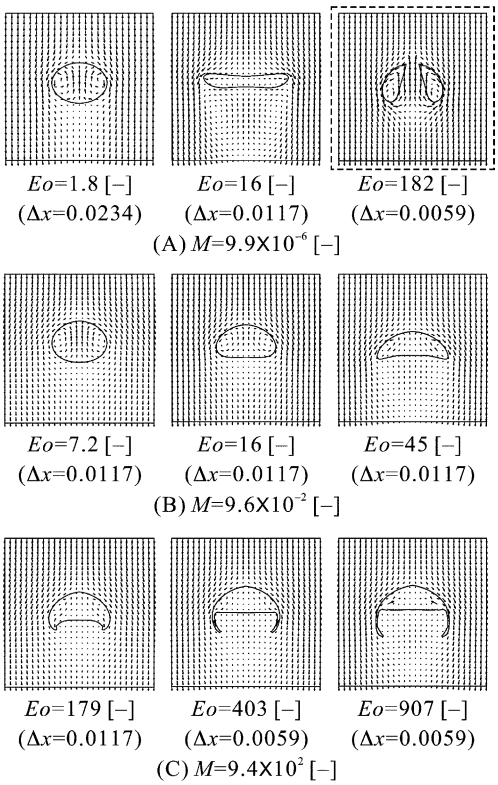

Fig. 6. Computational results for a variety of bubble rise motions.

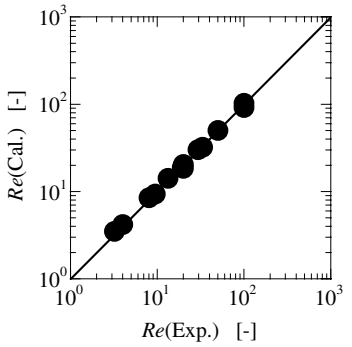

Fig. 7. Comparison of computed and experimental *Re*.

$M = 9.9 \times 10^{-6}$, it can be seen that the bubble begins to break up at the center (toroidal bubble); we will discuss results for high *Eo* and low *M* areas (the points marked by the squares in Fig. 1) in the next section. In general, the numerically predicted shapes are in good agreement with the diagram of Bhaga and Weber (1981) (Fig. 1): "oblate ellipsoid" bubble for $Eo = 1.8$, $M = 9.9 \times 10^{-6}$ and $Eo = 7.2$, $M = 9.6 \times 10^{-2}$; "disk-like" bubble for $Eo = 16$, $M = 9.9 \times 10^{-6}$; "skirted" bubble for $Eo = 403$ and 907, $M = 9.4 \times 10^{2}$; "oblate ellipsoidal cap" bubble for $Eo = 16$ and 45, $M = 9.6 \times 10^{-2}$, $Eo = 179$, $M = 9.4 \times 10^{2}$. For "oblate ellipsoidal cap" bubble area, the bubble terminal shape can depend on *Eo* and *M* numbers. The bubble shape result for $Eo = 179$ and $M = 9.4 \times 10^{2}$ is closer to a "dimpled ellipsoidal-cap" bubble presented by Grace et al. (1976) instead of "oblate ellipsoidal cap" bubble as predicted in Fig. 1. In Fig. 7, we present the comparison of the *Re* number for the results shown in Figs. 5 and 6. The black circles denote values obtained by the computations. As is clear from Fig. 7, our computed values for *Re* agree well with the observed values of *Re*.

4.3. Rising bubbles for "spherical-cap" bubble areas

In this section, we examine the effect of initial flow conditions on the resulting terminal bubble motion for "spherical-cap" bubble areas. As we have already shown in Fig. 6, the toroidal bubble for the condition of $Eo = 182$, $M = 9.9 \times 10^{-6}$ was reproduced numerically in starting the computation from the spherical shape. Fig. 8 shows numerical results obtained by changing initial bubble conditions. The computational targets (conditions of the dimensionless parameters) are the black squares shown in Fig. 1: (1) $Eo = 464$, $M = 6.5 \times 10^{-2}$ (one condition of the experiments by Hnat and Buckmaster (1976)); and (2) $Eo = 182$, $M = 9.9 \times 10^{-6}$. In Fig. 8, three kinds of initial bubble shapes are presented: the spherical bubble (condition 1) and deformed bubbles (conditions 2 and 3). For the two deformed bubble conditions, we performed our computations using data from previous computations of oblate ellipsoidal cap bubbles. We note that our initial conditions of a spherical bubble, or our initial conditions 2 and 3, are ideal conditions; but the point we wish to emphasize is that we can clearly establish the dependence of the initial flow condition on bubble motion. The computations in Fig. 8 were made using an interface thickness of $\varepsilon = 1.0\Delta x$. We remark that we had to be careful to compute on a sufficiently fine mesh so that the absolute interface numerical thickness, ε, was small enough in order to resolve the bubble

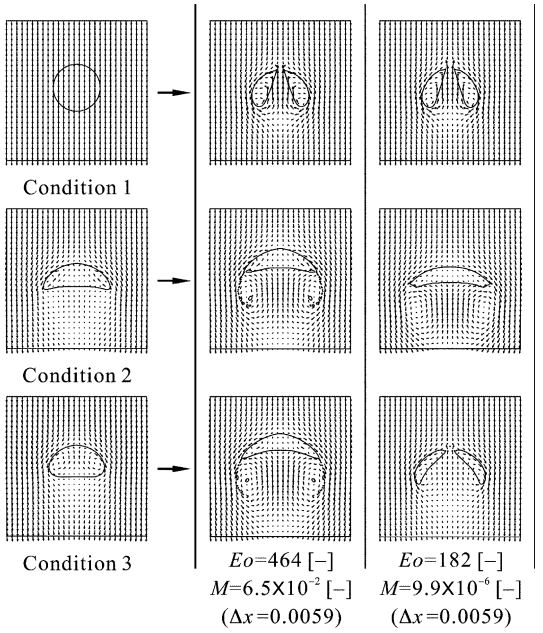

Fig. 8. Computational results of bubble rise motion depending on initial conditions for spherical-cap region.

dynamics. An underresolved calculation might result in a skirted bubble instead of a cap bubble. Also, an underresolved calculation might result in a toroidal bubble instead of an unsteady cap bubble. In all of our calculations, we verified the convergence of our results through grid refinement studies and through studies in which the interfacial thickness parameter, ε, is varied. Here, we illustrate examples of the dependency of the absolute interface numerical thickness on bubble shape in Fig. 9. In Fig. 9, three sets of figures with different interface numerical thicknesses are shown for each Eo and M condition. As for the case of $Eo = 182$, $M = 9.9 \times 10^{-6}$ (started from condition 2), it is obvious that the final bubble states are independent of the interface numerical thickness. The same fact was applicable to computations started from condition 3 (the terminal bubble shape is a toroidal bubble for condition 3). The results for the case of $Eo = 464$, $M = 6.5 \times 10^{-2}$ are slightly influenced by the interface numerical thickness as seen in Fig. 9. That is, the thickness of the skirted part becomes thinner as the absolute interface numerical thickness decreases, and it is expected that the skirted part will disappear as the mesh size $\Delta x^{\ell_{\max}}$ approaches 0. We observed the same "skirt thinning" phenomena for the case of $Eo = 464$, $M = 6.5 \times 10^{-2}$ using condition 3. For results started from condition 1, the bubbles break up at the center irregardless of the interface numerical thickness. In Fig. 8, what the numerical results make clear is that the final state of bubble motion is affected by the initial conditions. That is, we can verify that the bubble rise motion greatly depends on the initial conditions. For all the Eo and M conditions shown in Fig. 8 (unsteady cap region), the bubbles finally break up at the center when the computations are started from condition 1. Meanwhile, the bubbles never break up at the center when the computations are started using condition 2. The final state in these cases become a cap-shaped bubble. In contrast to the results for conditions 1 and 2, the results obtained using condition 3 depend on Eo and M conditions. In the case of condition 3 for $Eo = 181$,

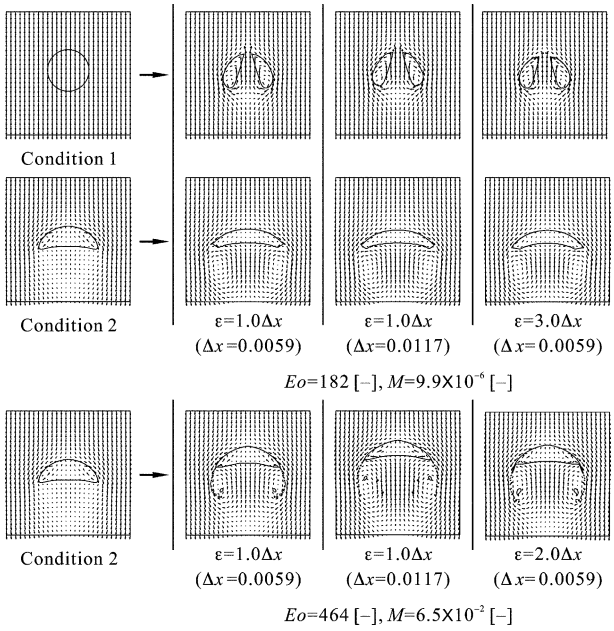

Fig. 9. The dependency of the absolute interface numerical thickness on bubble shape for spherical-cap region.

$M = 9.6 \times 10^{-2}$, the bubble breaks up at the center as is the case with condition 1. On the other hand, we obtain bubbles without break-up for $Eo = 464$, $M = 6.5 \times 10^{-2}$. In fact, for $Eo = 464$, $M = 6.5 \times 10^{-2}$, the resulting terminal bubble shape is independent of whether the bubble is started from condition 2 or 3, of course, with a spherical initial condition (condition 1), the terminal shape is unsteady and becomes a toroid. We remark that the terminal velocity (computed *Re*) is independent of whether the bubble ($Eo = 464$, $M = 6.5 \times 10^{-2}$) was started from condition 2 or 3.

Fig. 10 shows the comparison of computed and experimental *Re* numbers corresponding to the results in Fig. 8, except for the toroidal bubbles. The black squares are new points. It can be seen that the computed values for *Re* including the new points are a good match with the experimental values for *Re*.

4.4. Effect of initial flow conditions except for "spherical-cap" bubble areas

In Section 4.3, we considered the effect of initial flow conditions on the terminal bubble shape for high *Eo* and low *M* conditions where toroidal bubbles were reproduced numerically in starting from the spherical bubble condition. In this section, we shall focus on the effect of initial flow conditions for the conditions where the bubble rise motion predicted in Fig. 1 was able to be reproduced numerically using the spherical bubble condition. Fig. 11 shows the numerical results depending on three initial bubble conditions (the spherical bubble (condition 1) and deformed bubbles (conditions 2 and 3).) The bubble conditions in terms of the dimensionless numbers, *Eo* and *M*, are (1) $Eo = 1.8$, $M = 9.9 \times 10^{-6}$; and (2) $Eo = 16$, $M = 9.6 \times 10^{-2}$. From Fig. 11, it can be concluded that the final terminal bubble shape does not have a dependence on flow con-

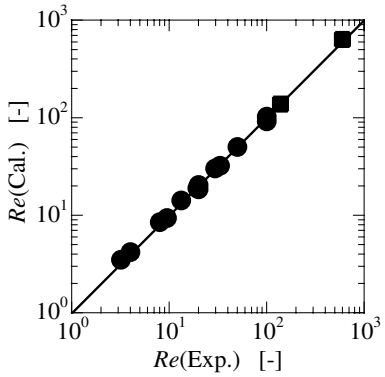

Fig. 10. Comparison of computed and experimental *Re* including the results for spherical-cap region.

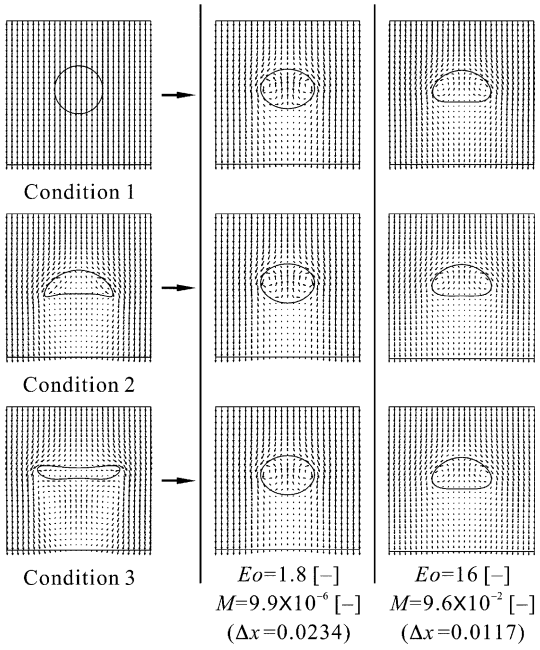

Fig. 11. Computational results of bubble rise motion depending on initial conditions for the cases where reasonable results were able to be obtained numerically using the spherical bubble condition.

ditions in the low *Eo* and high *M* areas. Furthermore, we observed that the terminal bubble rise speed is independent of the initial flow conditions. Making a comprehensive assessment of the effect of initial conditions for low *Eo* and relatively high *M* areas, we can expect that bubble motion is not subject to the initial bubble conditions. Therefore, in the region of low *Eo*, high *M*, of the graphical correlation in Fig. 1, the bubble motion is independent of the initial conditions.

Although we have only considered 2d, axisymmetric bubbles, as opposed to 3d bubbles, we have proved sufficiently in this study that bubble motion is dependent on the initial conditions for "spherical-cap" bubble areas (high *Eo*, low *M*).

5. Conclusions

We numerically considered the effect of initial bubble conditions on the resulting motion of a 2d-axisymmetric bubble rising in viscous Newtonian liquids using the CLSVOF method. As a result, it was shown that the motion of rising bubbles for "spherical-cap" bubble areas (high Eo and low M conditions) were influenced by the initial bubble conditions. That is, for these regions, we found some solutions to depend on initial bubble conditions/geometry: for the conditions of $Eo = 464,\ M = 6.5 \times 10^{-2}$ and $Eo = 182,\ M = 9.9 \times 10^{-6}$, the results of "spherical-cap" shape could be obtained when computations were started from deformed bubbles, and the bubbles with break-up could be numerically reproduced in starting from the spherical bubble. Regarding the regions except for spherical-cap bubble areas and 3d-nonlinear motion areas (very low M condition), we can say that bubble motion is not subject to the initial bubble conditions. In the dimensionless region of low Eo and very low M, it will be necessary to perform fully 3d-computations instead of the 2d-axisymmetric computations performed in this paper.

Acknowledgment

The authors would like to express our gratitude to Mr. D. Kikuchi for her helpful collaboration.

References

Best, J., 1993. The formation of toroidal bubbles upon the collapse of transient cavities. J. Fluid Mech. 251, 79–107.
Bhaga, D., Weber, M.E., 1981. Bubbles in viscous liquids: shapes, wakes and velocities. J. Fluid Mech. 105, 61–85.
Bunner, B., Tryggvason, G., 2002. Dynamics of homogeneous bubbly flows. Part 1. Rise velocity and microstructure of the bubbles. J. Fluid Mech. 466, 17–52.
Chen, L., Garimella, S.V., Reizes, J.A., Leonardi, E., 1999. The development of a bubble rising in a viscous liquid. J. Fluid Mech. 387, 61–96.
Clift, R.C., Grace, J.R., Weber, M.E., 1978. Bubbles, Drops and Particles. Academic Press, Tokyo.
Esmaeeli, A., Tryggvason, G., 1998. Direct numerical simulations of bubbly flows. Part 1. Low Reynolds number arrays. J. Fluid Mech. 377, 313–345.
Esmaeeli, A., Tryggvason, G., 1999. Direct numerical simulations of bubbly flows. Part 2. Moderate Reynolds number arrays. J. Fluid Mech. 385, 325–358.
Grace, J.R., Wairegi, T., Nguyen, T.H., 1976. Shapes and velocities of single drops and bubbles moving freely through immiscible liquids. Trans. Instn. Chem. Engrs. 54, 167–173.
Hnat, J.G., Buckmaster, J.D., 1976. Spherical cap bubbles and skirt formation. Phys. Fluids 19, 182–194.
Himeno, T., Watanabe, T., 1999. Numerical analysis of two-phase flow under microgravity condition. Trans. JSME Ser. B 65, 2333–2340 (in Japanese).
Hirt, C.W., Nichols, B.D., 1981. Volume of fluid method for the dynamics of free boundaries. J. Compt. Phys. 39, 201–225.
Li, Y., Zhang, J., Fan, L.-S., 2000. Discrete-phase simulation of single bubble rise behavior at elevated pressures in a bubble column. Chem. Eng. Sci. 55, 4597–4609.
Marten, K., Shariff, K., Psarakos, S., White, D.J., 1996. Ring bubbles of dolphins. Sci. Amer. 275, 83–87.
Ohta, M., Iwasaki, E., Obata, E., Yoshida, Y., 2003. A numerical study of the motion of a spherical drop rising in shear-thinning fluid systems. J. Non-Newtonian Fluid Mech. 116, 95–111.

Ohta, M., Haranaka, S., Yoshida, Y., Sussman, M., 2004. Three-dimensional numerical simulations of the motion of a gas bubble rising in viscous liquids. J. Chem. Eng., Jpn. 37, 968–975.

Puckett, E.G., Almgren, A.S., Bell, J.B., Marcus, D.L., Rider, W.J., 1997. A high-order projection method for tracking fluid interfaces in variable density incompressible flows. J. Comput. Phys. 130, 269–282.

Ryskin, G., Leal, L.G., 1984. Numerical solution of free boundary problems in fluid mechanics. Part 2. Buoyancy driven motion of a gas bubble through a quiescent liquid. J. Fluid Mech. 148, 19–35.

Son, G., 2001. A numerical method for bubble motion with phase change. Numer. Heat Transfer B 39, 509–523.

Sussman, M., 2003. A second order coupled level set and volume-of-fluid method for computing growth and collapse of vapor bubbles. J. Comput. Phys. 187, 110–136.

Sussman, M., Puckett, E.G., 2000. A coupled level set and volume-of-fluid method for computing 3d and axisymmetric incompressible two-phase flows. J. Comput. Phys. 162, 301–337.

Sussman, M., Smereka, P., 1997. Axisymmetric free boundary problems. J. Fluid Mech. 341, 269–294.

Sussman, M., Smereka, P., Osher, S., 1994. A level set approach for computing solutions to incompressible two-phase flow. J. Comput. Phys. 114, 146–159.

Sussman, M., Fatemi, E., Smereka, P., Osher, S., 1998. An improved level set method for incompressible two-phase flows. Comput. Fluids 27, 663–680.

Sussman, M., Almgren, A.S., Bell, J.B., Colella, P., Howell, L.H., Welcome, M.L., 1999. An adaptive level set approach for incompressible two-phase flows. J. Comput. Phys. 148, 81–124.

Tomiyama, A., Sou, A., Minagawa, H., Sakaguchi, T., 1991. Numerical analysis of a single bubble with VOF method. Trans. JSME Ser. B 57, 2167–2173 (in Japanese).

Tomiyama, A., Sou, A., Hosokawa, H., Sakaguchi, T., 1994. Three-dimensional detailed numerical simulation of bubbly flow in vertical square duct. Trans. JSME Ser. B 60, 2678–2685 (in Japanese).

Tomiyama, A., Celata, G.P., Hosokawa, S., Yoshida, S., 2002. Terminal velocity of single bubbles in surface tension force dominant regime. Int. J. Multiphase Flow 28, 1497–1519.

Walters, J.K., Davidson, J.F., 1963. The initial motion of a gas bubble formed in an inviscid liquid. Part 2. The three-dimensional bubble and the toroidal bubble. J. Fluid Mech. 17, 321–336.

Wu, M., Gharib, M., 2002. Experimental studies on the shape and path of small air bubbles rising in clean water. Phys. Fluids 14, L49–L52.

Yang, B., Prosperettia, A., Takagi, S., 2003. The transient rise of a bubble subject to shape or volume changes. Phys. Fluids 15, 2640–2648.